Multi-sided completion of C^2 bi-3 and C^1 bi-2 splines: a unifying approach

Kęstutis Karčiauskas[a], Jörg Peters[b,*]

[a] *Vilnius University, Lithuania*
[b] *University of Florida, USA*

Abstract

Traditionally the approach to filling n-sided holes differs substantially for bicubic C^2-splines vs biquadratic C^1-splines due to the 'primal' vs 'dual' interpretation of the control net that emphasises either n-valent vertices or n-sided facets. Here we propose a construction that unites the treatment of both types of spline surfaces, notably for non-4-valent vertices in a quad-layout. The primal-dual-agnostic multi-sided surfaces are of degree bi-4. Their main body can be chosen to be C^1 or C^2 and the remaining gap is filled by a tiny central G^1 cap.

Keywords: oven-odd degree, multi-sided spline surface, semi-structured spline, primal-dual, smooth shape, guided surface

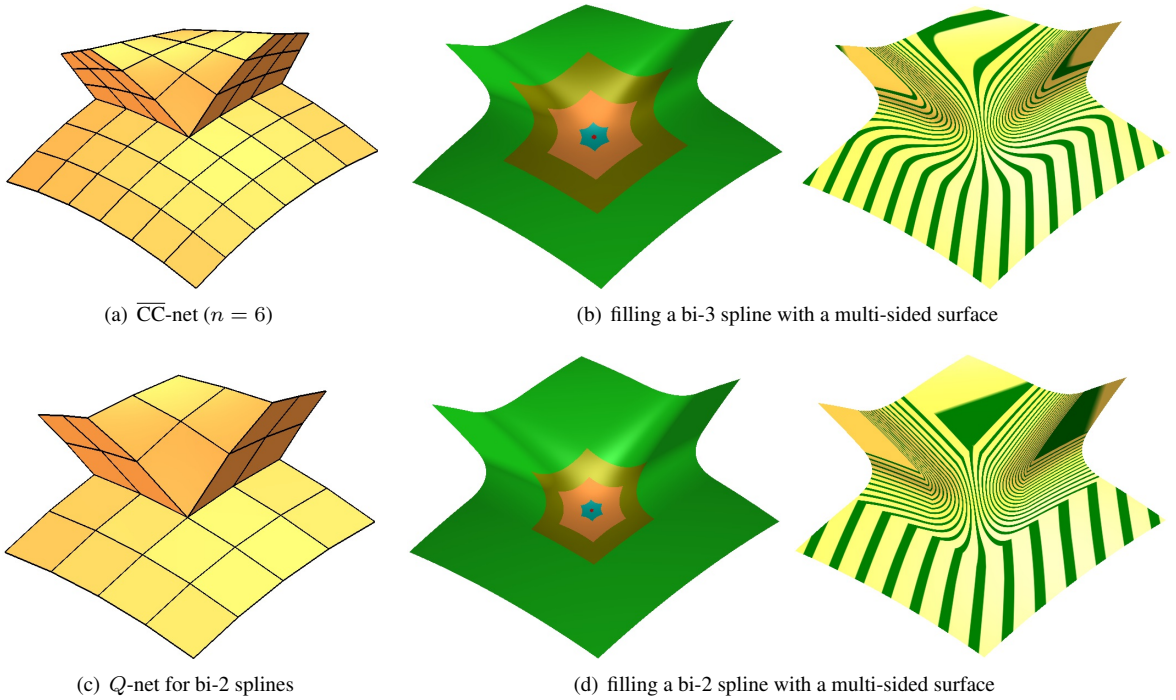

(a) $\overline{\text{CC}}$-net ($n = 6$) (b) filling a bi-3 spline with a multi-sided surface

(c) Q-net for bi-2 splines (d) filling a bi-2 spline with a multi-sided surface

Figure 1: (a) The 'primal' quad net (Catmull-Clark, short $\overline{\text{CC}}$-net) yields (b) a bi-cubic (bi-3) surface ring that is C^2-joined to a sequence of bi-quartic rings completed with a tiny bi-4 cap. (c) The quad net Q yields (d) a bi-quadratic (bi-2) surface ring that is C^1-joined to a sequence of bi-quartic rings completed with a tiny bi-4 cap. In both cases the multi-sided surfaces are constructed with the same algorithm. (*right*: highlight lines [BC94].)

*Corresponding author
Email addresses: kestutis.karciauskas@mif.vu.lt (Kęstutis Karčiauskas), jorg.peters@gmail.com (Jörg Peters)

1. Introduction

With their edges outlining preferred directions, quadrilateral meshes are widely used in the design of free-form surfaces. Interpreting grid-like sub-meshes as B-spline control nets transfers a coarse polyhedral design to a smooth, curved model. Good designers and good quadrangulation algorithms use a minimal number of irregularities where $n \neq 4$ quadrilaterals meet or the mesh forms an n-sided facet. Some irregularities are unavoidable, due to topological reasons, but more often they are introduced to align boundaries of polynomial pieces with preferred directions, e.g. when merging several tensored primitives into one surface.

For univariate splines, switching to higher-degree shape functions, a.k.a. p-refinement, simply amounts to re-interpreting the control points as weights of higher-degree B-splines. For spline surfaces, the type of irregularity – n-valent vertex or n-sided facet – changes with the interpretation of the control net. If the net is interpreted as controlling a uniform tensor-product C^2 bicubic (bi-3) spline, then n-valent vertices are prevalent and the control net is often called 'primal'. If the quad-net is interpreted as controlling a uniform tensor-product C^1 biquadratic (bi-2) spline, then n-sided facets arise and the control net is considered 'dual'. Even though both types of irregularities cause multi-sided holes in spline surfaces, the treatment of irregularities in primal and dual nets starkly differs and switching between them would require re-meshing to accommodate the dual and primal layout. As a case in point, Doo-Sabin (DS) subdivision [DS78] and Catmull-Clark (CC) subdivision [CC78] do not mix freely.

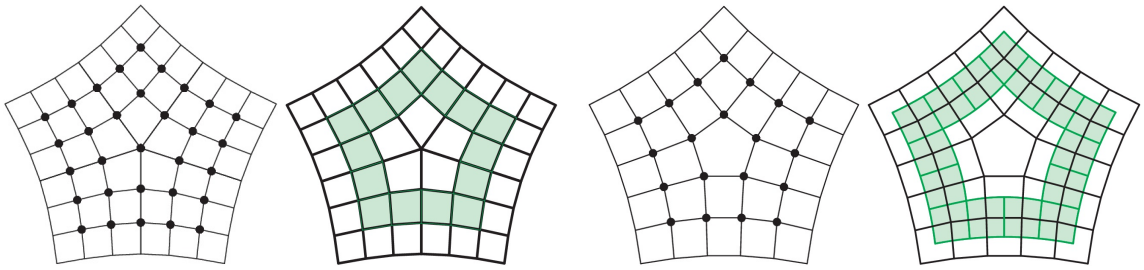

(a) $\overline{\text{CC}}$-net and • of CC-net (b) $\overline{\text{DS}}$-net and • of DS-net

Figure 2: (a) Primal layout and green bi-3 spline ring (b) dual layout and green bi-2 spline ring.

The unified multi-sided cap construction presented in the following accommodates both primal and dual configurations by applying the principle of guided surfacing to both. We call the quad mesh in Fig. 2 a a $\overline{\text{CC}}$-net in reference to Catmull-Clark subdivision and the subset of control points marked •, a CC-net. The CC-net suffices for the cap construction. The $\overline{\text{CC}}$-net additionally defines a regular bi-3 spline ring surrounding the cap to be able to judge the transition from a bi-3 spline surface to the cap based on the shared layout.

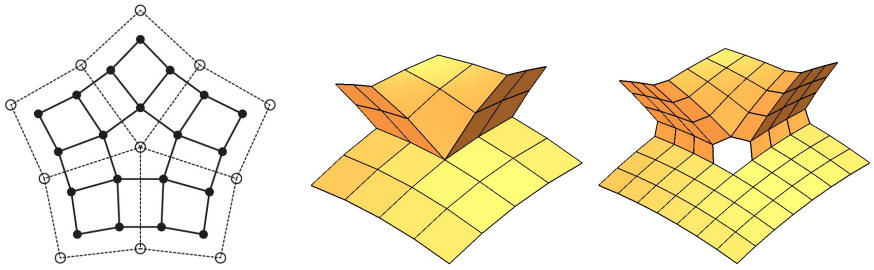

(a) quad- $\rightarrow DS$-net (b) Q-net $\rightarrow$ extended $\overline{\text{DS}}$-net

Figure 3: (a) Conversion of the Q-net to a DS-net via bi-2 knot insertion. (b) Bi-2 knot insertion applied to entire Q-net yields an extended $\overline{\text{DS}}$-net (here Q-net from Fig. 1 c).

Since CC-nets are common in design, we want to alternatively be able to interpret CC-nets as control-nets for C^1 bi-2 splines and so make high-end surface algorithms more widely applicable without interfering with the designer's

intentions as conveyed by the control net layout. Bi-2 splines are dual to the CC-net in the sense that the images of their knot-line crossings (corners of the polynomial pieces) coincide with averages of quad vertices (the center of quad facets). To avoid a confusion with the primal interpretation, we re-name the CC-net in the dual context a Q-net. We propose to address the question, what to do at the central point, by applying one local, *virtual* regular bi-2 spline knot insertion. The knot insertion (see Fig. 3 a) generates the control points marked • in Fig. 2 b; these form the DS-net in Fig. 2 b, in reference to Doo-Sabin subdivision. The larger $\overline{\text{DS}}$-net defines a regular bi-2 spline ring to assess the transition between cap and the surrouding bi-2 spline surface. The conversion of the Q-net yields three layers of quads, see Fig. 3 b, i.e. a $\overline{\text{DS}}$-net extended by one extra layer. These quads define two rings of regular bi-2 splines surrounding the cap. Since the two rings are created by subdivision, their shape is identical to that of the innermost regular ring defined directly by the Q-net: the layers are the innermost ring – with each polynomial patch split into 2×2 pieces.

Contributions The unified construction generates a well-shaped surface of degree bi-4 that reminds of a few steps of Catmull-Clark or Doo-Sabin subdivision, see Fig. 1 . The construction is a hybrid that combines the advantages of subdivision algorithms (simple refinability due to C^1 and C^2 transitions) and the good shape of G-splines while avoiding the respective shortcomings: the infinite recursion for subdivision, and the absence of a simple homogeneous refinement for G-splines due to the special treatment of G-edges. The surfaces consist of a user-chosen number of nested bi-4 surface rings that scale down towards the remaining hole. Typically three rings suffice to shrink the size of the remaining hole by almost two orders of magnitude. For most modeling applications and much of engineering analysis the final smooth bi-4 G-spline cap then need not be further refined.

While non-trivial to derive, the resulting algorithm is affine in the control net: for given n and contraction speed σ (high speed yields wide, fast-contracting surface rings) it can be implemented as the multiplication of the control net nodes with a sequence of pre-calculated matrices. That is, evaluation of these splines for multi-sided surfaces is only moderately slower than evaluation of splines over regular meshes.

Overview. Section 2 and Section 3 review, for completeness, known techniques that will serve as building blocks of the new algorithm in Section 4. The new algorithm combines and adds to the building blocks. In more detail, after a review of related work, Section 2 lists the concepts and tools to define the unified multi-sided construction: sampling of Hermite data and geometric smoothness. Section 3 reviews the basic ideas underlying Guided Surfacing, in the context of the unified construction. Section 4 defines the algorithm: constructing a guiding surface and the transition to rapidly contracting guided surface rings capped by a tiny central surface piece. Section 4 also states the properties of the resulting surfaces. The section also describes how the construction can be efficiently implemented in terms of pre-calculated matrices. Section 5 justifies algorithmic choices via examples and Section 6 discusses alternatives and limitations.

1.1. Related work

Interpreting the nodes of a grid-like mesh as control points of a bi-cubic (bi-3) tensor-product spline is a simple and low-cost way to obtain high-quality smooth surfaces. Analogously, interpreting the nodes as control points of uniform tensor-product C^1 biquadratic (bi-2) splines yields even simpler smooth surfaces that, while of lower quality than bi-3 splines, suffice for many applications, e.g. designing internal surfaces.

The generalizations of knot insertion to fill multi-sided holes, Doo-Sabin subdivision [DS78] and Catmull-Clark subdivision [CC78] suffer from shape artifacts. Catmull-Clark surfaces typically have pinched highlight lines (see [BC94]) when modeling higher-order saddles; and [KPR04] showed that even for convex input meshes the limit shape is hyperbolic. Tuning subdivision weights [CADS09, MM18] to adjust the eigenstructure and hence the differential geometry jet at the extraordinary point; directly prescribing leading parts of the eigenstructure [LFS16]; or prescribing the limit jet directly, geometrically by a guide surface (which implies the wanted eigenstructure) as in Guided Subdivision [KP07] can remove targeted artifacts, but at the cost of a more complex algorithm to generate contracting rings. [TSH+20] illustrated that contracting rings, just like regular spline surfaces, can be built from piecewise polynomials of differing degree and joined with different levels of smoothness, so called multi-degree B-splines.

Alternatively, surface constructions have been proposed that do not restrict themselves to the standard polynomial spline paradigm: generalizing Gregory patches [HK18], transfinite interpolation [VSR12] and highly-smooth surfaces have been proposed for multisided surfaces [SVR14, SV18, HK20b, HK20a]

Another alternative to subdivision surfaces are G-splines [HM90, Pet02]. G-splines consist of a finite number of piecewise polynomials that join by change of variables (reparameterization) and can yield high quality surfaces [LS08, KP16]. By the result [GP15], and demonstrated e.g. in [KNP16, NKP16], G-splines are directly suitable for engineering analysis. The complexity of refining G-splines [KP17] and the difficulty of designing with the resulting finer degrees of freedom triggered the investigation of hybrid constructions that complete a finite number of nested, C^k-joined surface rings with an n-sided G-spline cap. [KP18] yields almost everywhere curvature continuous multi-sided surfaces of degree bi-6. This paper focuses on a unified construction of high-quality, n-sided surfaces of much lower degree, bi-4, that can fill holes both in bi-2 C^1 and bi-3 C^2 surfaces and so generalizes the approach of [KP20].

2. Definitions and Setup

The construction of well-shaped surfaces has advanced to the point where a standard set of techniques and building blocks can be assembled – with care – to form the task-specific solution. This section defines the basic setup, how to sample derivatives to form L-shaped pieces that combine to form surface rings and how to convert from B-spline form to BB-form – specific to the the primal-dual task at hand. The section also reviews the characteristic parameterization of Catmull-Clark subdivision and the notion of geometric continuity (G^1 continuity).

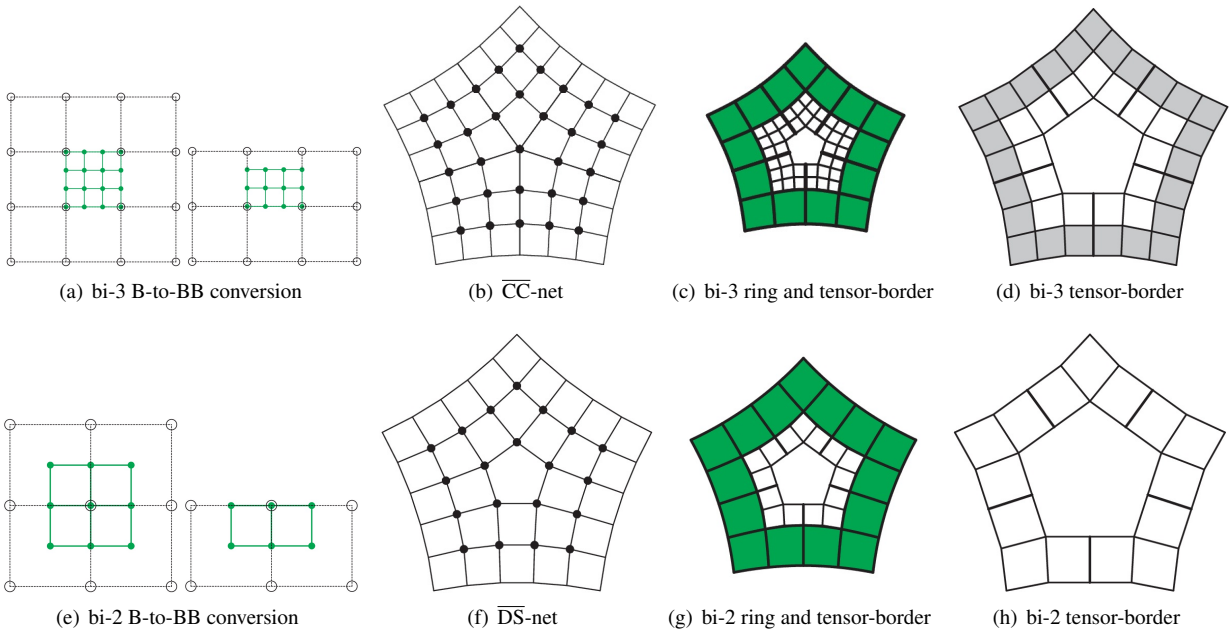

(a) bi-3 B-to-BB conversion (b) $\overline{\text{CC}}$-net (c) bi-3 ring and tensor-border (d) bi-3 tensor-border

(e) bi-2 B-to-BB conversion (f) $\overline{\text{DS}}$-net (g) bi-2 ring and tensor-border (h) bi-2 tensor-border

Figure 4: B-to-BB conversion and tensor-borders $\mathbf{t}$ as Hermite input data. (a,e) Circles ○ mark B-spline control points, solid disks ● mark BB-coefficients for *left* full patch, *right* tensor-border. (b,f) The input nets define respectively, a green ring of (c) C^2-connected bicubic patches, (g) C^1-connected biquadratic patches. The partial net ● defines a tensor-border $\mathbf{t}$, displayed as finer inner grids on white background in (c), (g). (d) shows a close-up of $\mathbf{t}$ to emphasize its use as C^2 extension of a bi-3 ring and (h) for a C^1-extension of a bi-2 ring.

2.1. Conversion from B-spline to BB-form and tensor-borders

The surfaces consist of tensor-product patches of bi-degree d (short bi-d) in Bernstein-Bézier form (BB-form), see e.g. [Far88]:

$$\mathbf{f}(u,v) := \sum_{k=0}^{d}\sum_{\ell=0}^{d} \mathbf{f}_{k\ell} B_k^d(u) B_\ell^d(v), \quad 0 \le u, v \le 1.$$

Here $B_i^d(t) := \binom{d}{i}(1-t)^{d-i}t^i$ are the Bernstein polynomials of degree d and $\mathbf{f}_{ij}$ are the BB-coefficients. Connecting $\mathbf{f}_{ij}$ to $\mathbf{f}_{i+1,j}$ and $\mathbf{f}_{i,j+1}$ wherever possible yields the *BB-net*. A useful operation on polynomials in BB-form is to split them into two pieces, say a left half and a right half, by the well-known *de Casteljau algorithm* [Far88].

The vertices, marked in Fig. 4 juxtaposes the input for the bi-d constructions for $d = 2$ and $d = 3$. Any $(d+1) \times (d+1)$ sub-grid with control points marked $\circ$ in Fig. 4 a,e can be interpreted as the control points of a uniform bi-d B-spline. The *B-to-BB conversion* expresses the spline in bi-d BB-form illustrated by the green BB-net in Fig. 4 a,e. Conversion of a partial sub-grid yields a partial BB-net, see Fig. 4 a,e,*right*, defines position and first (and for the case $d = 3$ second) derivatives across an edge, called *tensor-border* and denoted $\mathbf{t}$. B-to-BB conversion of the full net creates a bi-d surface ring (green in Fig. 4 c,g) and a (white underlaid) tensor-border.

Fig. 4 d,h juxtapose the first-order tensor-borders that form the input for the unified construction. Fig. 4 h displays the bi-2 tensor-border corresponding to the inner grid in Fig. 4 g. Fig. 4 d displays the bi-3 tensor-border, of which the first-order Hermite data, the gray-underlaid strip corresponding to the inner grid of Fig. 4 c, will play a special role. The extraordinary point adds important information in the bi-3 case.

2.2. *Sampling derivatives to form tensor-borders and L-shapes*

Jets of derivatives of patches or tensor-borders $\mathbf{f}$ can be represented by BB-subnets, see Fig. 5 . BB-subnets corresponding to jets of $\mathbf{f}$ in different locations can be combined (assembled) into new patches as illustrated in Fig. 5 b,c. Where subnets overlap the jet-information is averaged, see Fig. 5 c. The operator that samples the kth order jet of a function $\mathbf{f}$ at suitable locations and assembles a patch or an L-shape as llustrated in Fig. 5 is denoted H^k. L-shapes can be joined in a cycle to form surface rings. For good quality, it pays to adjust bi-4 L-shapes to join C^2 where they meet along sector-separating curves as illustrated in for the vertical edge above 1 in Fig. 5 d, *right*. Fig. 5 d, *right*, provides the weights for a formula to overwrite the column of BB-coefficients marked $\uparrow$ (corresponding to the middle column of the light blue BB-subnet in Fig. 5 d, *left*). Applying this formula also to the circled $\bullet$ of the neighboring sector to the right makes the L-shapes join C^2. Specifically, for the column marked by $\uparrow$ the new value is the affine combination with weights $[1, 4, -1]/4$ of the remaining BB-subnet columns to both sides of the sector-separating curve.

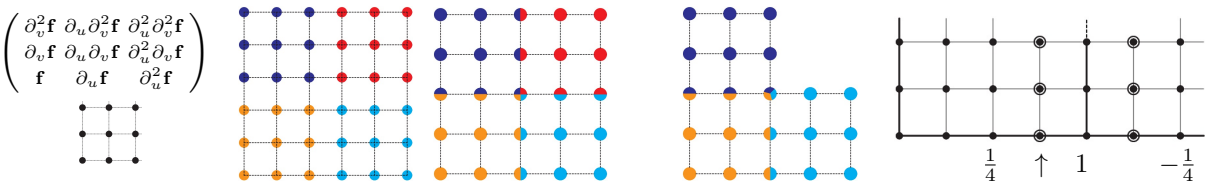

(a) $\partial_u^i\mathbf{f}$ in BB-form (b) bi-5 (c) bi-4 (d) bi-4 L-shape and C^2 correction

Figure 5: Hermite data (partial derivatives converted to BB-form) and Hermite operators H^k, $k = 5, 4$: (a,b) full patch; (c) L-shaped bi-4 tensor-border and its C^2 correction: the circled BB-coefficients (see $\uparrow$ for the left three) are the $\frac{1}{4}$, 1, $\frac{-1}{4}$ average of their neighbors.

2.3. *Adjustable Speed Subdivision and the characteristic parameterization* $\bar{\chi}_\sigma$

The subdominant eigenvalue of subdivision governs the contraction speed of the subdivision rings towards the limit. The subdominant eigenvalue of bi-3 Adjustable Speed Subdivision [KP09] with 'speed' parameter $\sigma \in (0..1)$ is

$$\lambda_\sigma := \frac{\tilde{\sigma}}{2}((1+\mathsf{c})\sigma^2 + 2\tilde{\sigma} + \sigma\sqrt{(1+\mathsf{c})((1+\mathsf{c})\sigma^2 + 4\tilde{\sigma})}), \quad \mathsf{c} := \cos(2\pi/n),\ \tilde{\sigma} := 1-\sigma. \tag{1}$$

The choice $\sigma := \frac{1}{2}$ replicates Catmull-Clark subdivision.

The *left* BB-nets of Fig. 6 a,b,c, display characteristic maps χ_σ for one sector and $n = 5$. In the analysis of Catmull-Clark subdivision the maps χ_σ contain key analytic information. By contrast, in guided subdivision, the corresponding tensor-borders $\bar{\chi}_\sigma$, Fig. 6 , *right* are more important. The gray underlaid BB-coefficients of χ_σ are the result of splitting $\bar{\chi}_\sigma$ in the ratio $\sigma : \tilde{\sigma}$ (see Fig. 6 b). We normalize the characteristic maps so that the corner BB-coefficients (marked as $\diamond$ in Fig. 6 a) are at the distance 1 from the center $\circ$. While different σ result in different χ_σ, their tensor-borders $\bar{\chi}_\sigma$ although slightly different, look alike. This allows a gentle switch to higher speeds. The λ_σ-scalability of characteristic tensor-borders will enable an efficient implementation of the sampled guided rings in the next section.

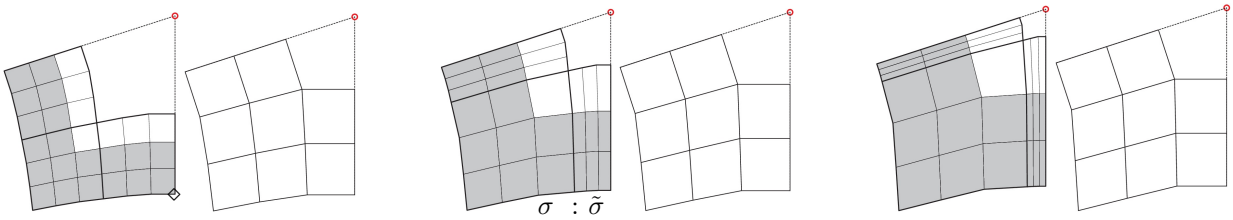

(a) $\sigma := \frac{1}{2}$ (CC) (b) $\sigma := \frac{3}{4}$ (c) $\sigma := \frac{7}{8}$

Figure 6: Characteristic parameterizations (*left*) χ_σ and their tensor-borders (*right*) $\bar{\chi}_\sigma$ of one sector in relation to the irregular point ∘.

2.4. G^1 continuity

Definition 1. *Two sufficiently smooth regular surface pieces* $\tilde{\mathbf{f}}$ *and* $\mathbf{f}$ *sharing a boundary curve* $\mathbf{e}$ *join* G^1 *if there exists a suitably-oriented and non-singular reparameterization* $\rho : \mathbb{R}^2 \to \mathbb{R}^2$ *so that for* $k = 0, 1$*, the partial derivatives* $\partial^k \tilde{\mathbf{f}}$ *and* $\partial^k(\mathbf{f} \circ \rho)$ *agree along* $\mathbf{e}$*.*

Throughout, we will choose $\mathbf{e}$ to correspond to surface patch parameters $(u, 0 = v)$. Then the relevant Taylor expansion (up to degree 1) of the reparameterization ρ with respect to v is

$$\rho := (u + b(u)v, a(u)v). \tag{2}$$

By the chain rule of differentiation, this yields the well-known G^1 constraints in terms of univariate scalar functions $a(u)$, $b(u)$ and the vector-valued functions $\mathbf{f}(u, 0)$, $\tilde{\mathbf{f}}(u, 0)$

$$\partial_v \tilde{\mathbf{f}} = a(u)\partial_v \mathbf{f} + b(u)\partial_u \mathbf{f}. \tag{3}$$

Practical multi-sided constructions obey a natural combinatorial symmetry. This combinatorial symmetry holds for constructions in the paper: L-shapes are constructed by diagonally symmetric rules and neighboring sectors are constructed without bias with respect to their shared sector-separating curve: that is, if $\tilde{\mathbf{f}}$ and $\mathbf{f}$ are exchanged in (3) then the constraints remain the same. No bias implies that $a(u) := -1$.

3. Basic Principles of Guided Surfacing

A guide surface outlines the intended shape of the final surface. In this section, we specialize known techniques as building blocks to construct a guide surface $\mathbf{g}$ for the task at hand. We define a consistent central expansion, derive $\mathbf{g}$ from the data, repeatedly sample $\mathbf{g}$ to create a sequence of rapidly contracting surface rings, and, after a few steps, cap the sequence with a tiny G^1 multi-sided surface piece. The advantage of this multi-step approach, both for design and analysis, is that the resulting surface consists of finitely many piecewise polynomials and is straightforward to refine (by knot insertion) up to the tiny cap. A new component, borrowed from the recent construction [KP20], is the use of an intermediate map $\mathbf{p}$ in Section 3.1 that defines the shape in a primal-dual agnostic fashion.

3.1. A piecewise bi-4 G^1 map $\mathbf{p}$ and its unconstrained BB-coefficients

The challenge here is to derive one proto-guide suitable for both primal and dual configurations. We call $\mathbf{p}$ a proto-map since it remains symbolic until certain unconstrained BB-coefficients have been specified. Fig. 7 a shows the layout of $\mathbf{p}$: each of the n sectors of $\mathbf{p}$ is a single polynomial patch of degree bi-4. The green-underlaid strips of BB-coefficients guarantee geometric continuity with the input tensor-borders constructed – according to Section 2.2 – along the green boundary $\mathbb{m}^{s-1}$, $\mathbb{c}^s$, $\mathbb{m}^s$. The grey-underlaid strips guarantee geometric continuity across the sector-separating curves $\mathbb{o}$, $\mathbb{m}^s$. The BB-coefficients marked as ∘ represent Hermite data up to order 2 at the extraordinary point. These *quadratic expansions* $\mathbf{q}^s$ are derived from a single map $\tilde{\mathbf{q}}$ of total degree 2, by reparameterization with a map τ defined below.

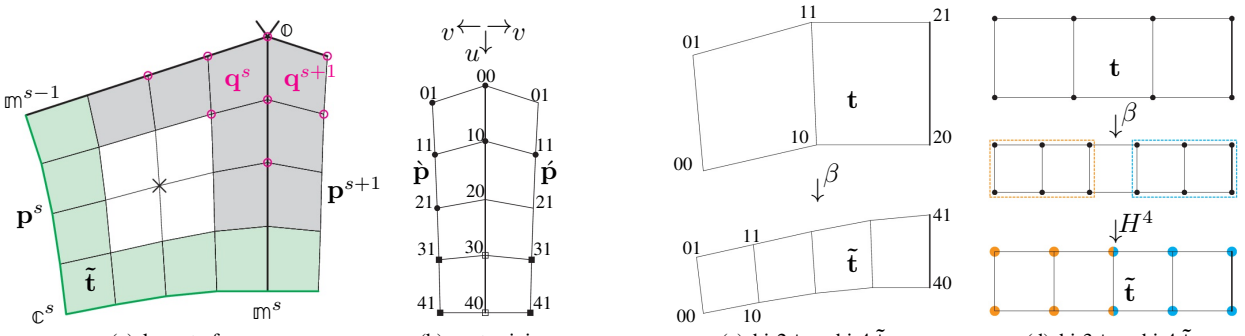

Figure 7: Proto-map $\mathbf{p}$ from tensor-border $\mathbf{t}$. (a) BB-net of the bi-4 map $\mathbf{p}$. (b) The BB-coefficients enforcing the G^1 constraints between sectors, i.e. along the edge $[\mathfrak{o}, \mathbb{m}^s]$ in (a); BB-coefficients that remain unconstrained are marked $\bullet$. (c) Reparameterization β of bi-2 tensor-border $\mathbf{t}$ to $\tilde{\mathbf{t}}$ as defined in [KP20] and (d) its adjustment to the primal case, to transform the bi-3 tensor-border $\mathbf{t}$ to the bi-4 tensor-border $\tilde{\mathbf{t}} := H^4(\mathbf{t} \circ \beta)$.

Fig. 7 b displays the subnet of BB-coefficients involved in the G^1-constraints (3) between the sectors. Here $a(u) := -1$, $b(u) := 2\mathsf{c}(1-u)$, $\mathsf{c} := \cos\frac{2\pi}{n}$. The constrained BB-coefficients are

$$\acute{\mathbf{p}}_{i0} := \grave{\mathbf{p}}_{i0}, i = 0, \dots, 4, \quad \acute{\mathbf{p}}_{01} := -\grave{\mathbf{p}}_{01} + 2\mathsf{c}\grave{\mathbf{p}}_{10} + 2(1-\mathsf{c})\grave{\mathbf{p}}_{00}, \quad \acute{\mathbf{p}}_{21} := -\grave{\mathbf{p}}_{21} + (2-\mathsf{c})\grave{\mathbf{p}}_{20} + \mathsf{c}\grave{\mathbf{p}}_{30},$$
$$\grave{\mathbf{p}}_{20} := \frac{(3\mathsf{c}-4)\grave{\mathbf{p}}_{10} + 2(\grave{\mathbf{p}}_{11} + \acute{\mathbf{p}}_{11})}{3\mathsf{c}}, \quad \grave{\mathbf{p}}_{30} := \frac{2(\grave{\mathbf{p}}_{31} + \acute{\mathbf{p}}_{31}) - \mathsf{c}\grave{\mathbf{p}}_{40}}{4-\mathsf{c}}, \quad \grave{\mathbf{p}}_{40} := \frac{\grave{\mathbf{p}}_{41} + \acute{\mathbf{p}}_{41}}{2}.$$

The assignment of $\acute{\mathbf{p}}_{01}$ enforces tangent plane continuity at the extraordinary point; the relation that determines $\grave{\mathbf{p}}_{30}$ triggers the reparameterization $\beta := [u, a(u)v]$, $a(u) := \frac{2}{2-\mathsf{c}}(1-u)^2$ of the input tensor-border $\mathbf{t}$, Fig. 4 . Among the possible choices for $b(u)$, $b(u) = 0$ is not only the simplest option but also yields the best shape. The unconstrained middle BB-coefficient $\mathbf{p}_{22}$, marked as $\times$ in Fig. 7 a, is defined as

$$\mathbf{p}_{22} := \frac{1}{2}\Big(\frac{2}{3}(\mathbf{p}_{21} + \mathbf{p}_{23}) - \frac{1}{6}(\mathbf{p}_{20} + \mathbf{p}_{24})\Big) + \frac{1}{2}\Big(\frac{2}{3}(\mathbf{p}_{12} + \mathbf{p}_{32}) - \frac{1}{6}(\mathbf{p}_{02} + \mathbf{p}_{42})\Big),$$

where the pattern $\frac{2}{3}(\mathbf{p}_1 + \mathbf{p}_3) - \frac{1}{6}(\mathbf{p}_0 + \mathbf{p}_4)$ indicates reduction to degree 3, a choice that reduces oscillations in the surface. The resulting bi-4 map is internally formally G^1 regardless of the choice of the unconstrained BB-coefficients marked as $\bullet$ in Fig. 7 b.

The reparameterization τ of [KP20, Sec4.1] can be interpreted as a specific piecewise bi-4, rotationally-symmetric map $\tau : (\mathbb{R}^2)^n \to \mathbb{R}^2$ that satisfies the G^1 constraints above (with τ in place of $\mathbf{p}$). Fig. 7 a shows one sector of τ for $n = 5$. Since τ is planar, the quadratic expansion $\mathbf{q}$ is not needed in its construction. The map τ approximates χ_σ (shown in Fig. 6) and will be used as a reparameterization, i.e. to map planar domains to one another, and specifically to derive the quadratic expansion $\mathbf{q}$ from the composition of a quadratic map $\tilde{\mathbf{q}}$ with τ.

3.2. A C^1 guide surface $\mathbf{g}$

Guided surfacing typically employs maps of total degree k over a triangular domain. Various k and internal continuities can be chosen. Maps of total degree are prefered over tensor-product maps since they allow an efficient sampling of Hermite data when constructing a contracting sequence of surface rings. Here we can choose one of the simplest, a map of total degree 5 borrowed from [KP20]. We then derive a specific $\mathbf{g}$ for the unified approach to optimally fit $\mathbf{g} \circ \tau$ to the known $\mathbf{p}$.

Fig. 8 a displays the structure of the C^1 map $\mathbf{g}$ of total degree 5 over a pentagonal domain D. The quadratic $\tilde{\mathbf{q}}$ (in degree-raised form) at the center is defined by six BB-coefficients $\bullet$ of the first sector. Iterative application of the C^1 stencil $\mathbf{s} := (1 - \frac{1}{\mathsf{c}})\mathbf{n} + \frac{1}{2\mathsf{c}}(\mathbf{e} + \mathbf{w})$ along the sector-separating curve, see Fig. 8 b, zippers the sectors together to form a C^1 map. The BB-coefficients marked $\bullet$ remain unconstrained, as are those marked as $\circ$ that do not affect the C^1-join between the sectors.

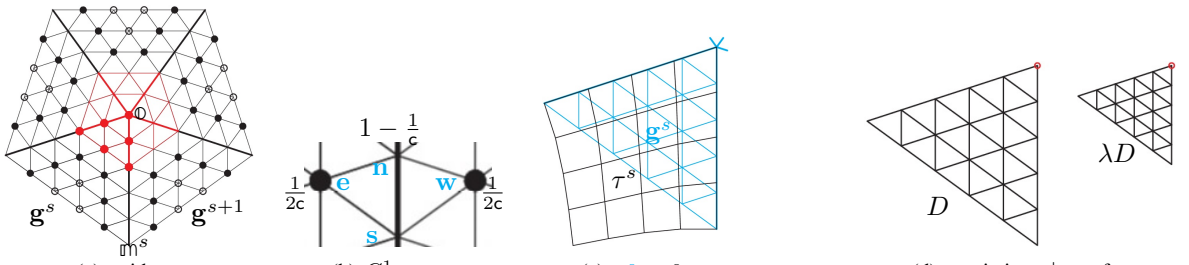

(a) guide $\mathbf{g}$ (b) C^1 pattern (c) $\mathbf{g}^s \circ \tau^s$ (d) restriction $\mathbf{g}|_{\lambda D}$ of $\mathbf{g}$

Figure 8: (a) C^1 guide of total degree 5. The red sub-net represents a quadratic map $\tilde{\mathbf{q}}$ in degree-raised form. (b) C^1 pattern between adjacent sectors. (c) Sampling the guide $\mathbf{g}^s$ of sector s with parameterization τ^s. (d) The restriction $\mathbf{g}|_{\lambda D}$ of $\mathbf{g}$ to the scaled domain ($\circ$ marks the origin.)

Restricting $\mathbf{g}$ to the scaled domain λD (see Fig. 8 d) yields the map $\mathbf{g}|_{\lambda D}$. The BB-coefficients of $\mathbf{g}|_{\lambda D}$, are obtained by applying the (uni-variate) de Casteljau's algorithm in two directions, see e.g. [Far88]. [KP18] Let $\ell+1$ be the maximal number of spline rings to be generated, typically $\ell = 2$ or $\ell = 3$, and s label the n sectors. Then

$$\mathbf{g}^{1,s} := \mathbf{g}^s \text{ and iterate } \mathbf{g}^{r+1,s} := \mathbf{g}^{r,s}|_{\lambda_{\sigma_r D}},\ r = 1, \ldots, \ell \tag{4}$$

where $\lambda_{\sigma_r D}$ indicates the contraction of the domain D according to the chosen sequence σ of contraction speeds $(\sigma_1, \sigma_2, \ldots, \sigma_\ell) \in [0..1]$ that select subdominant eigenvalues by (1).

3.3. Constructing adjustable multi-sided surface rings $\mathbf{r}^r$ from tensor-borders

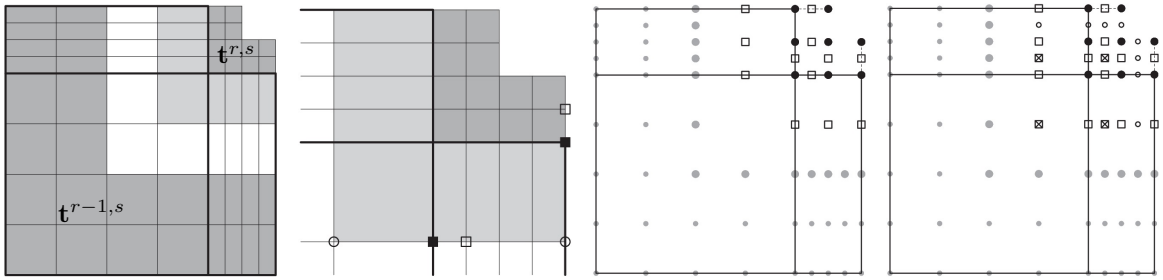

(a) C^1 ring (b) C^1 extension (c) C^2 ring, 1st □ (d) C^2 ring, 2nd □

Figure 9: Construction of the bi-4 surface sector $\mathbf{p}^{r-1,s}$ by combining the tensor-borders $\mathbf{t}^{r-1,s}$ and $\mathbf{t}^{r,s}$.

The guide surface $\mathbf{g}$ captures the intended shape. A sequence of contracting rings approximates the guide ever more closely by combining the prolongation of the existing outer surface with the samples of Hermite data from $\mathbf{g}$. The resulting sequence is akin to classical subdivision surfaces, and suitable both for refined geometric manipulations and engineering analysis.

The tensor-borders $\mathbf{t}^{r-1}$ and $\mathbf{t}^r$ are joined to form a nested sequence of surface rings $\mathbf{r}^r$ of degree bi-4 that is by choice either C^1 or C^2. Consider one sector s of ring r as in Fig. 9. By splitting the tensor-border sector $\mathbf{t}^{r-1,s}$ in the ratio $\sigma_{r-1} : 1-\sigma_{r-1}$, the sequence can be advanced faster or slower towards the central point, see Fig. 9 a. For a C^1-joined sequence, $\mathbf{r}^{r-1,s}$ combines the once-split $\mathbf{t}^{r-1,s}$ with the C^1 extension of $\mathbf{t}^{r,s}$ 'backwards' towards $\mathbf{t}^{r-1,s}$ (gray in Fig. 9 a,b) by applying, in both parameters, the stencil $\circ := \frac{1}{1-\sigma_{r-1}}\blacksquare - \frac{\sigma_{r-1}}{1-\sigma_{r-1}}\square$ as marked in the zoomed-in view Fig. 9 b.

For a C^2-joined sequence, $\mathbf{r}^{r-1,s}$ combines the split tensor-border $\mathbf{t}^{r-1,s}$ with data modified from $\mathbf{t}^{r,s}$ as follows. Fig. 10 illustrates a rule or stencil that enforces a non-uniform C^2 join of two Bézier curves meeting with ratio σ:$\tilde{\sigma}$, $\tilde{\sigma} := 1 - \sigma$, at the end point marked by ● and e_1:

$$e_0 := \frac{\tilde{\sigma}}{2},\ e_1 := \frac{1}{2\tilde{\sigma}},\ e_2 := 1 - e_0 - e_1;\ \tilde{e}_i(\sigma) := e_{2-i}(\tilde{\sigma}), \quad \tilde{\sigma} := 1 - \sigma.$$

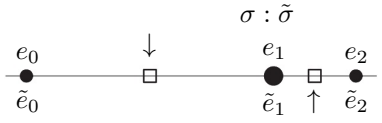

Figure 10: Stencil for non-uniform C^2-join at ●.

In Fig. 9 c, gray disks mark the innermost BB-coefficients of the split tensor-border $\mathbf{t}^{r-1,s}$ and • mark a subset of the BB-coefficients of tensor-border $\mathbf{t}^{r,s}$. Applying the stencil of Fig. 10 in each direction to two black bullets • and one grey bullet generates the BB-coefficients shown as hollow squares. Applying the stencil to two hollow squares and one grey bullet generates the crossed squares in Fig. 9 d. Applying the C^2-correction rule of Fig. 5 d, *right*, generates the BB-coefficients marked ○. The so-modified tensor-border replaces $\mathbf{t}^{r,s}$ for generating the next ring.

3.4. A tiny central cap $\hat{\mathbf{p}}$

We avoid the infinite recursion of subdivision surfaces, by contracting fast, and completing the surface by a bi-4 cap analogous to [KP20]. The structure of this cap $\hat{\mathbf{p}}$ is displayed in Fig. 11 a: each sector consists of one 2×2, internally C^1 macro-patch. The BB-coefficients displayed as • join the cap C^1 to the last guided ring (unlike for $\mathbf{p}$, no reparameterization is needed). The magenta BB-coefficients are defined by the quadratic expansion of $\mathbf{g}$ at the extraordinary point. The gray-underlaid BB-coefficients insure a G^1-join between the sectors (the BB-coefficients marked • in Fig. 11 b are initially unconstrained.)

Not only is the first-order smoothness of the cap natural in the context of bi-2 surfaces, but, as we wil show, it also yields shape on par with more complex, formally curvature continuous constructions with C^2 and G^2 transitions.

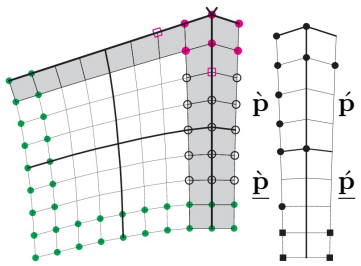

(a) $\hat{\mathbf{p}}$ (b) G^1

Figure 11: Structure of central cap $\hat{\mathbf{p}}$ and G^1-constraints.

4. The unified construction algorithm

We now assemble the technical building blocks developed in the previous sections. To derive the sequence of pre-calculated matrices that map the input CC-net or Q-net to the BB-coefficients of the polynomial surface pieces, we construct in order

- 4.1 a multi-sided, internally G^1 surface $\mathbf{p}$ of degree bi-4 that outlines the final surface;
- 4.2 a multi-sided, internally C^1 surface $\mathbf{g}$ of total degree 5 that outlines the final surface in a way that is suitable for the unified construction;
- 4.3 a transition ring $\mathbf{r}^0$ that blends to the surrounding surface;
- 4.4 a sequence of adjustable-speed multi-sided surface rings $\mathbf{r}^r, r = 1,\dots,\ell$ and
- 4.5 a final tiny n-sided central cap $\hat{\mathbf{p}}$.

For $d = 3$ and $n > 4$ we apply one CC subdivision step before computing $\mathbf{p}$ and $\mathbf{g}$. For a CC-net, $d = 3$ and $n = 3$, or for a DS-net and $d = 2$, we contract $\mathbf{g}$ once $\mathbf{g} \leftarrow \mathbf{g}|_{\lambda_{\frac{1}{2}} D}$, as illustrated in Fig. 8 d.

The factored derivation of the guide in Steps a,b separates the initial shape $\mathbf{p}$ from a representation $\mathbf{g}$ that is convenient for contructing nested surface rings $\mathbf{r}^r$.

4.1. Determining a multi-sided, internally G^1 *surface* $\mathbf{p}$ *of degree bi-4 that outlines the final surface*

To determine the unconstrained BB-coefficients of $\mathbf{p}$ from Section 3.1 we proceed, with $\grave{\mathbf{p}}_{ij} = \mathbf{p}^s_{ij}$, $\acute{\mathbf{p}}_{ij} = \mathbf{p}^{s+1}_{ji}$, as follows. Fig. 7 c,d illustrate the construction of $\tilde{\mathbf{t}} := H^4(\mathbf{t} \circ \beta)$. For $d = 2$, the first-order expansion across the boundary $\partial_v(\mathbf{t} \circ \beta)$ is of degree 4 in the u-direction. The operator $H^4(\cdot \circ \beta)$ therefore preserves the first-order Hermite data and $\tilde{\mathbf{t}}$ is the tensor-border $\mathbf{t}$, reparameterized. For $\deg = 3$, the degree of $\partial_v(\mathbf{t} \circ \beta)$ is 5 in the u-direction and only the boundary curve is preserved. Let $\mathbf{t}$ be the tensor-border (green-underlaid in Fig. 7 a) of the DS-net if $d = 2$ and CC-net if $d = 3$. For $d = 3$, we set $\tilde{\mathbf{q}}^0_1$ to be the extraordinary point of Catmull-Clark subdivision improved for $n = 3$ as in [KP16]. Then the remaining $n + 8 - d$ unconstrained BB-coefficients $\{\tilde{\mathbf{q}}^0_i, i = d-1,\dots,6$ and $\mathbf{p}^s_{21}$, $s = 0,\dots,n-1\}$ are set to minimize $\mathcal{F}_{d+1}$ over all n bi-4 patches $\mathbf{p}^s$ where the functional

$$\mathcal{F}_k f := \int_0^1 \int_0^1 \sum_{i+j=k, i,j\geq 0} \frac{k!}{i!j!} (\partial_s^i \partial_t^j f(s,t))^2 \, ds \, dt$$

penalizes variation of kth derivatives.

The shape of $\mathbf{p}$ is good. In the bi-2 setting, $\mathbf{p}$ will join the surrounding spline smoothly – although not with the wanted top surface quality. In the bi-3 setting, $\mathbf{p}$ will only connect C^0 to the surrounding spline surface. These flaws do not matter since $\mathbf{p}$ only determines the interior shape of the final multi-sided surface while the transition to the surrounding surface is designed more carefully in Section 4.3.

4.2. The C^1 guide surface $\mathbf{g}$

The center point $\mathbb{o}$ of $\mathbf{g}$ (see Fig. 12) is the center point of $\mathbf{p}$. Denote by Γ the $5+9n$ free BB-coefficients: 5 marked $\bullet$, $6n$ marked $\bullet$ and $3n$ marked $\circ$. Then $\mathbf{a}^s := H^5(\mathbf{g}^s \circ \tau^s)$ is a bi-5 patch in the unknowns Γ. Denote by $\tilde{\mathbf{f}}^s$ the s-th sector of $\mathbf{p}$ degree-elevated to bi-5. Then the unconstrained BB-coefficients $\bullet$ and $\circ$ of $\mathbf{g}$ are set by minimizing over Γ, for all i, j and sectors s, the sum of squared distances $|\mathbf{a}^s_{ij} - \tilde{\mathbf{f}}^s_{ij}|^2$.

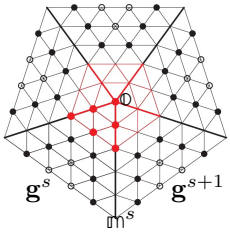

Figure 12: C^1 guide of total degree 5 (Fig. 8 a).

4.3. Constructing the transition ring $\mathbf{r}^0$

For the remainder of this section the operator H^4 includes the C^2-correction of the L-shaped tensor-borders defined in Fig. 5 d; and *extending 'backwards'* means constructing a tensor-border not towards the center $\mathbb{o}$ but towards the periphery as in Fig. 13 a, light gray.

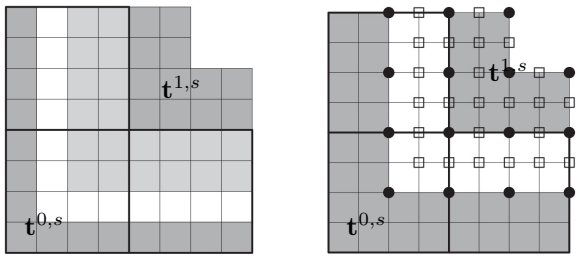

(a) transition to bi-2 (b) transition to bi-3

Figure 13: One sector $\mathbf{r}^{0,s}$ of the bi-4 transition ring $\mathbf{r}^0$ is obtained by combining the input tensor-border $\mathbf{t}^{0,s}$ and the guide-derived tensor-border $\mathbf{t}^{1,s}$.

The ring $\mathbf{r}^0$ transitions from a surrounding bi-2 or a bi-3 surface to a guided ring. We set $\sigma_0 := \frac{1}{2}$ and denote as $\mathbf{t}^{0,s}$ the sector s of the input tensor-border (representing Hermite data of order $d-1$, degree-raised to 4). The ring $\mathbf{r}^0$ combines the evenly-split $\mathbf{t}^0$ with the *backwards extension* of $\mathbf{t}^1 := H^4(\mathbf{g}^1 \circ \bar{\chi}_{\sigma_0})$.

For $d = 2$ the extension is C^2 (see Fig. 13 a). For $d = 3$ the extension is made C^2 by placing the BB-coefficients, marked as $\square$ in Fig. 13 b, according to the stencil of Fig. 10 with $\sigma = 1/2$, i.e. the uniform stencil in Fig. 5 d. The so-modified tensor-border replaces the original $\mathbf{t}^{1,s}$ for generating the next ring.

4.4. Construction of the main body

Applying for $r = 1, \ldots, \ell+1$ the sequence of surface rings $\mathbf{r}^r$ of Section 3.3 with $\mathbf{t}^{r,s} := H^4(\mathbf{g}^r \circ \bar{\chi}_{\sigma_{r-1}})$ forms the main body. The rings join, by choice, either C^1 or C^2. Section 5 investigates the (negative!) impact of increased formal smoothness on the surface quality.

For valencies, $n = 3, 5, 6$, the speed sequence $\sigma := (\frac{3}{4}, \frac{7}{8})$ produces three well-shaped guided rings $\mathbf{r}^0$, $\mathbf{r}^1$, $\mathbf{r}^2$. The remaing hole is as tiny as after six steps of Catmull-Clark subdivision. Section 5 investigates the impact of σ on the surface quality.

4.5. Summary

The construction can be summarized as repeatedly combining Hermite data of the surrounding surface with an ever smaller part of a fixed map $\mathbf{g}$, itself derived from $\mathbf{p}$. The surface then follows the shape of $\mathbf{g}$ but with a smoother transitions than $\mathbf{p}$ until is it capped by the tiny central cap $\hat{\mathbf{p}}$ of Section 3.4.

Both the guide and the unified construction are primal/dual agnostic, except for some minor technical differences when linking to either a bi-2 or a bi-3 surface. Proposition 1 collects the properties established in the preceding subsections.

Proposition 1. *(i) For $d \in \{2, 3\}$ the transition ring $\mathbf{r}^0$ is internally C^{d-1} and joins C^{d-1} to the surrounding C^{d-1} spline and C^2 with the main body.*
(ii) The rings $\mathbf{r}^r$, $r > 0$ of the main body are internally C^2 and can be joined C^1 or C^2, as preferred.
(iii) The central cap is internally G^1 and joins C^1 with the last ring.

4.6. Implementation

The algorithm's steps 4.1–4.5 are implemented as the multiplication of the control net nodes by (a sequence of) pre-calculated matrices. Due to construction symmetry, by cyclically permuting the net, formulas are only needed for one sector. The number of input nodes N is $6n + 1$ if $d = 3$ and $4n$ if $d = 2$. Therefore the construction of the $\binom{7}{5} = 21$ BB-coefficients of one sector of $\mathbf{g}$ can be implemented as a multiplication by a matrix of size $21 \times N$, precomputed, for the most common $n = 3, 5, 6, 7, 8$. Contracting the $\mathbf{g}$ then maps a sector to a refined copy by a matrix representing de Casteljau's algorithm applied twice.

Again taking advantage of the structural symmetry, the BB-coefficients of the L-shaped tensor-border $H^4(\mathbf{g}^{r+1} \circ \bar{\chi}_{\sigma_r})$ without C^2 correction can be computed by multiplication with a pre-calculated matrix $M(n, \sigma_r)$ that maps the 21 BB-coefficients of the polynomial $\mathbf{g}$ to the 21 BB-coefficients of the L-shaped bi-4 tensor-border (cf. Fig. 5 c).

Finally, the BB-nets of the four pieces of the tiny cap are linearly computed from the reparameterized BB-net of $\mathbf{g}$ and have $5 \times 5 = 25$ BB-coefficients each. The size and purpose of the matrices are summarized in Table 1.

map	separately for each	size of matrix
$\mathbf{g}$	n	$21 \times N$
$\mathbf{g} \to \mathbf{g}\vert_{\lambda_{\sigma.D}}$		21×21
L-shape*	n, σ^r	21×21
tiny cap	4 pieces	25×21

Table 1: Matrices for efficient implementation.

5. Examples and Choices

To compare the surfaces for primal and dual input, we choose a $\overline{\text{CC}}$-net for $d = 3$ and its CC-subnet as Q-net for $d = 2$; see Fig. 3 . Regular bi-2 or bi-3 spline patches are green and the tiny cap red. The main body is generated by the same algorithm and is by default C^1. For $d = 3$ and $n > 4$, we compare $\mathbf{g}$ to two alternative options denoted as $\dot{\mathbf{g}}$ and $\ddot{\mathbf{g}}$. The guide $\dot{\mathbf{g}}$ omits the Catmull-Clark refinement step before creating $\mathbf{p}$ (but contracts once $\dot{\mathbf{g}} \leftarrow \dot{\mathbf{g}}\vert_{\lambda_{\frac{1}{2}D}}$ just like $\mathbf{g}$ for $n = 3$). The option $\ddot{\mathbf{g}}$ first applies an extra Catmull-Clark refinement step and then replicates $\dot{\mathbf{g}}$, creating an additional regular bi-3 ring in the process. Comparison will justify the default choice $\mathbf{g}$.

The convex net Fig. 14 for $n = 3$ and speed sequence $(\frac{3}{4}, \frac{7}{8})$ yields one transition ring, two main body rings and a tiny cap. Despite the very fast contraction, no shape artifacts are observed, so that this speed sequence is selected as the default for $n = 3$. Fig. 15 shows a plane with one of its $n = 6$ sectors translated up. Such perturbed primitive shapes are challenging since minute oscillations can be noticed. Fig. 15 c,d display the default construction with speed sequence $(\frac{3}{4}, \frac{7}{8})$. Fig. 15 e reveals an oscillation in the transition (see ↑) when selecting the $\dot{\mathbf{g}}$ option; for $\ddot{\mathbf{g}}$ no oscillation is visible, see Fig. 15 f.

However the next input net demonstrates that $\ddot{\mathbf{g}}$, too, fails as a guide for high quality surfaces. The convex $n = 6$ input net of Fig. 16 is close to parabolic. Now $\dot{\mathbf{g}}$ (Fig. 16 c) is better but $\ddot{\mathbf{g}}$ (Fig. 16 d) is worse than the default

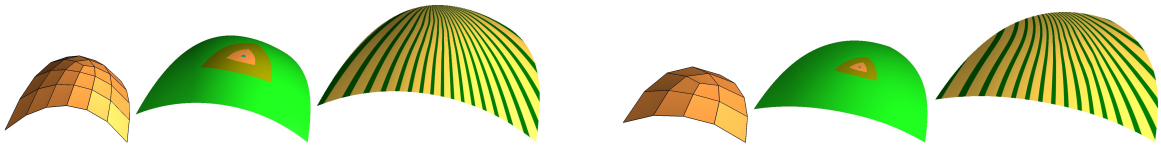

(a) bi-3 (b) bi-2

Figure 14: Convex shape test for $n := 3$: input net, surface layout, highlight lines. Speed sequence: $(\frac{3}{4}, \frac{7}{8})$.

(Fig. 16 b). The differences are caused by 'first step subdivision artifacts' [ADS11] whose progression generates ripples in any Catmull-Clark surface. Zooming in on the last guided ring and the tiny cap, the default construction with speed sequence $(\frac{3}{4}, \frac{7}{8})$ and C^1, respectively C^2 main bodies in Fig. 16 f is juxtaposed with the superior outcomes of the sequence $(\frac{3}{4}, \frac{3}{4}, \frac{3}{4})$ in Fig. 16 g. We note that for both sequences, the C^1 version has straighter highlight lines, hence a more desirable highlight line distribution than the C^2 version! This surprising fact holds up over numerous other test inputs. In Fig. 16 i, for $d = 2$, the clearly visible transition from the regular ring to the multi-sided surface is due to the sharp transitions between the *regular* bi-2 patches, i.e. not caused by the unified construction. An alternative, shown in Fig. 16 j, is discussed in Section 6.1.

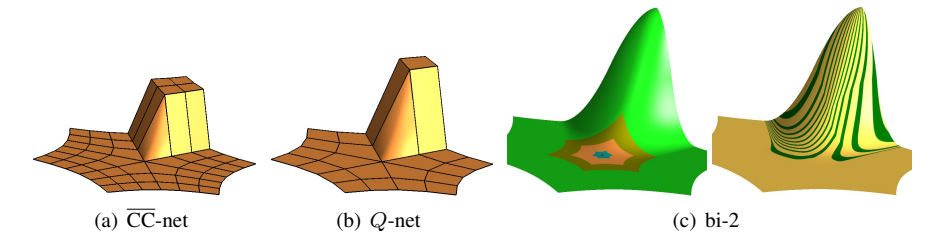

(a) $\overline{\text{CC}}$-net (b) Q-net (c) bi-2

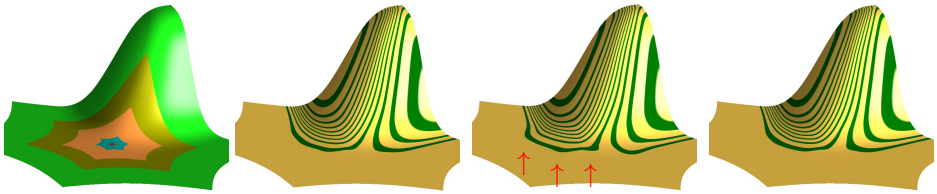

(d) bi-3 (e) $\dot{\mathbf{g}}$ (f) $\ddot{\mathbf{g}}$

Figure 15: The input net is a plane with one of $n = 6$ sectors translated up – for speed sequence $(\frac{3}{4}, \frac{7}{8})$.

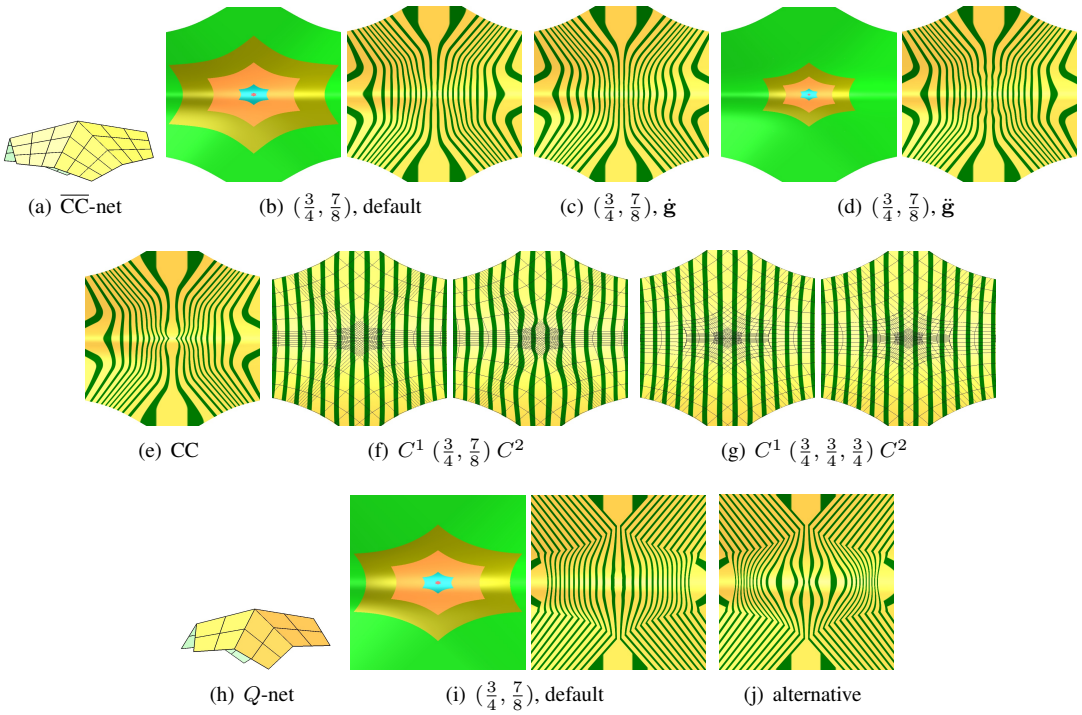

(a) $\overline{\text{CC}}$-net (b) $(\frac{3}{4}, \frac{7}{8})$, default (c) $(\frac{3}{4}, \frac{7}{8})$, $\dot{\mathbf{g}}$ (d) $(\frac{3}{4}, \frac{7}{8})$, $\ddot{\mathbf{g}}$

(e) CC (f) C^1 $(\frac{3}{4}, \frac{7}{8})$ C^2 (g) C^1 $(\frac{3}{4}, \frac{3}{4}, \frac{3}{4})$ C^2

(h) Q-net (i) $(\frac{3}{4}, \frac{7}{8})$, default (j) alternative

Figure 16: Convex net, $n = 6$. *top*, *middle*: $d = 3$, *bottom*: $d = 2$. (f,g): BB-nets are overlaid on the highlight lines.

Fig. 17 shows a smooth blend of $n = 7$ planes. The speed sequence $(\frac{3}{4}, \frac{3}{4}, \frac{3}{4})$ yields high quality in Fig. 17 b, whereas Catmull-Clark subdivision exhibits the typical pinching of the highlight lines near the extraordinary point, see Fig. 17 c,f. Fig. 17 d shows the intermediate guide $\mathbf{p}$ in red, with overlaid BB-net. The guide is only C^0-connected to the outer bi-3 surface. While the shape reflects the design intent, the ↑ points to a kink in the highlight lines between the sectors and ↓ in the transition from regular bi-3 ring to $\mathbf{p}$. By contrast, the same zoom in Fig. 17 e on the default unified surface Fig. 17 b reveals no artifacts. The zoom in Fig. 17 f on the Catmull-Clark surface Fig. 17 c emphasizes the artifacts already visible in the large. For $d = 2$, the default construction Fig. 17 h is contrasted with Doo-Sabin subdivision, Fig. 17 i, and Augmented Bi-2 subdivision [KP15b], Fig. 17 j. Augmented Bi-2 subdivision has weaker oscillations in the highlight lines than Doo-Sabin subdivision, but stronger ones than the default construction.

Fig. 18 zooms in on the tiny cap and the last ring(s) for input of valence $n = 10$. This and other high valence examples show that very high speed $\sigma_r := \frac{7}{8}$ reduces the surface quality while speed sequences with $\sigma_r := \frac{3}{4}$ yield acceptable highlight lines.

6. Discussion

6.1. Guide selection

For $d = 3$, $\mathbf{g}$ can be constructed directly from the input Hermite data. But for $d = 2$, direct initialization – via the characteristic tensor-border of Catmull-Clark subdivsion or Augmented Bi-2 subdivision – fails to produce convex surfaces where expected, see oscillations in Fig. 16 j. While this negative outcome does not preclude the existence of a simpler initialization for $d = 2$, it would imply separate treatment of bi-2 and bi-3 scenarios.

The guide in [KP19] can also be considered two-stage, e.g. akin to using first $\mathbf{p}$ and then $\mathbf{g}$, since it leverages an earlier G-spline construction [KP15a]. However, the surface is *bi*-5, more complex and requires larger pre-calculated matrices with 36 bi-5 BB-coefficients in place of 21 for our construction of total degree 5 (see Table 1). One can also consider [MM18] as a guide. However, [MM18] requires strong separation of irregular nodes and so does not allow tight configurations as in Fig. 20 e, below. (Separating irregular nodes by additional Catmull-Clark steps also typically reintroduces shape artifacts.) Moreover, the layout of the contracting rings in [MM18] is, as for any

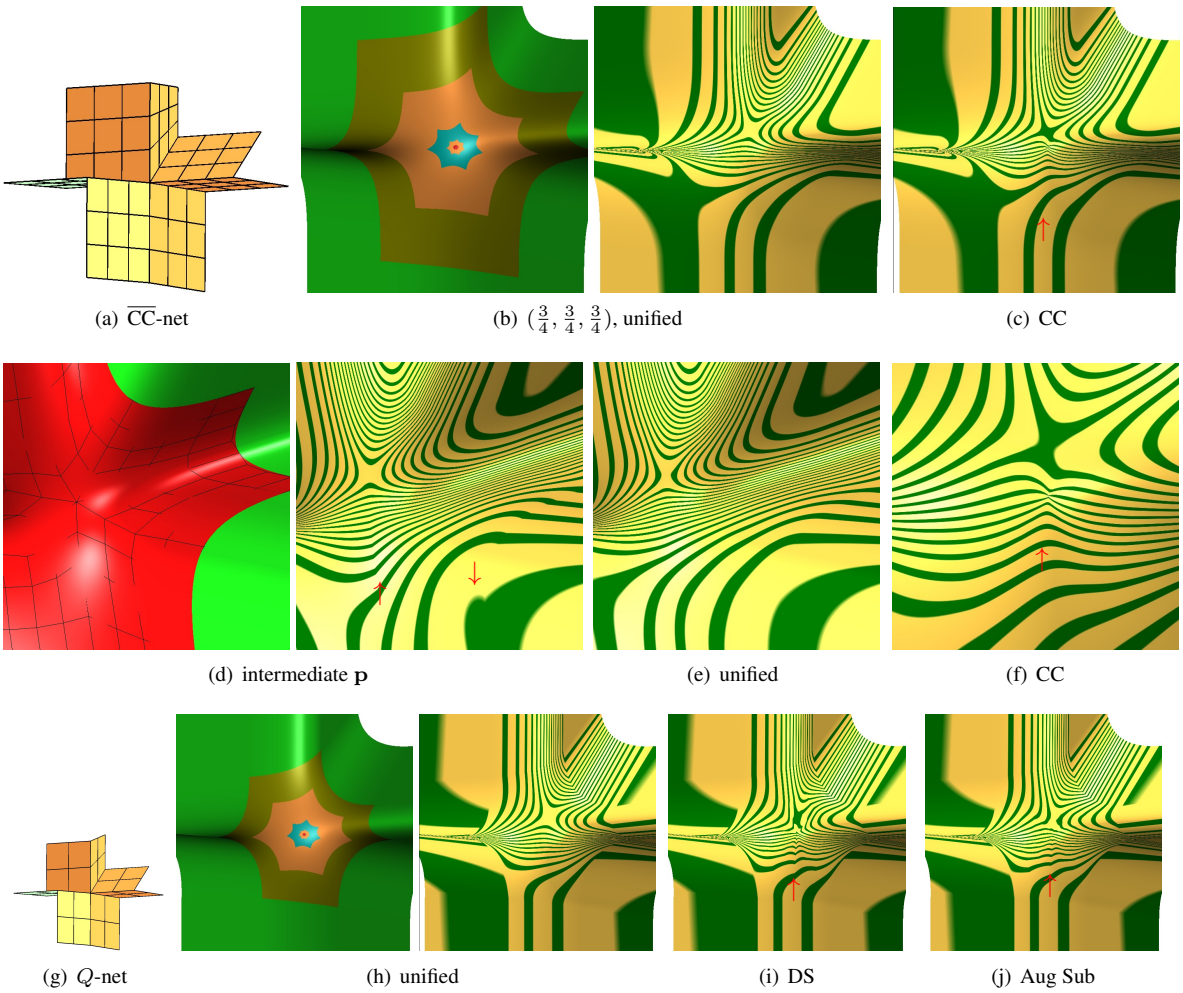

(a) $\overline{\text{CC}}$-net (b) $(\frac{3}{4}, \frac{3}{4}, \frac{3}{4})$, unified (c) CC

(d) intermediate $\mathbf{p}$ (e) unified (f) CC

(g) Q-net (h) unified (i) DS (j) Aug Sub

Figure 17: Valence $n := 7$, speed sequence $(\frac{3}{4}, \frac{3}{4}, \frac{3}{4})$. First two rows: $d = 3$, bottom row: $d = 2$. (enlarge pdf to see flaws ↑) CC = Catmull-Clark Subdivision; DS = Doo-Sabin Subdivision; Aug Sub = Augmented Bi-2 Subdivision.

curvature-bounded bi-3 subdivision scheme, more complex than for Catmull-Clark, without offering rapid contraction as our construction does. In principle, any construction of good shape can serve as guide. The challenge is to carefully sample the shape to avoid distortion. Sampling location and footprint, and placement in the final construction are key to good outcomes.

6.2. Tight configurations

Refinement accomodates tight configurations: the input mesh Fig. 19 a has no 4-sided facet. A single dual refinement (here Doo-Sabin) yields a net with overlapping DS-nets so that no bi-2 patch separates the bi-4 caps. But even a single Doo-Sabin step harms the resulting shape. Augmented Bi-2 subdivision [KP15b] achieves the same separation but improves the shape to the point that already the map $\mathbf{p}$ itself can serve as a final surface for some applications Fig. 19 c,e,f.

Fig. 20 a displays a quad mesh of genus 2 with 8 irregular nodes of valence 5, namely the vertices of the cube that connects two tori. Unlike the preceding examples, the irregular nodes are surrounded by only a single layer of quads, fewer than in a Q-net. In the primal (bi-3) setup the irregular nodes must be separated. One Catmull-Clark refinement is applied to Fig. 20 a to obtain Fig. 20 e. Unlike the preceding examples, the irregular nodes of this primal mesh are surrounded by only a CC-net, not by a $\overline{\text{CC}}$-net. In both cases the speed sequence is chosen to be $(\frac{3}{4}, \frac{7}{8})$ and

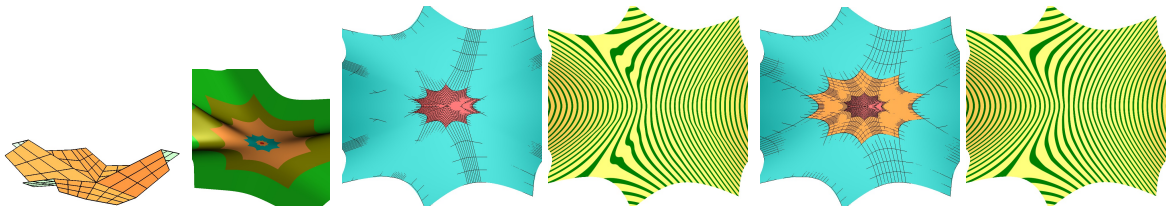

(a) CC-net (b) layout (c) $(\frac{3}{4}, \frac{7}{8})$ (d) $(\frac{3}{4}, \frac{3}{4}, \frac{3}{4})$

Figure 18: Wavy shape, $n = 10$, $d = 3$, C^1 main body. (c,d) innermost ring and tiny cap for (c) very fast and (d) fast contraction.

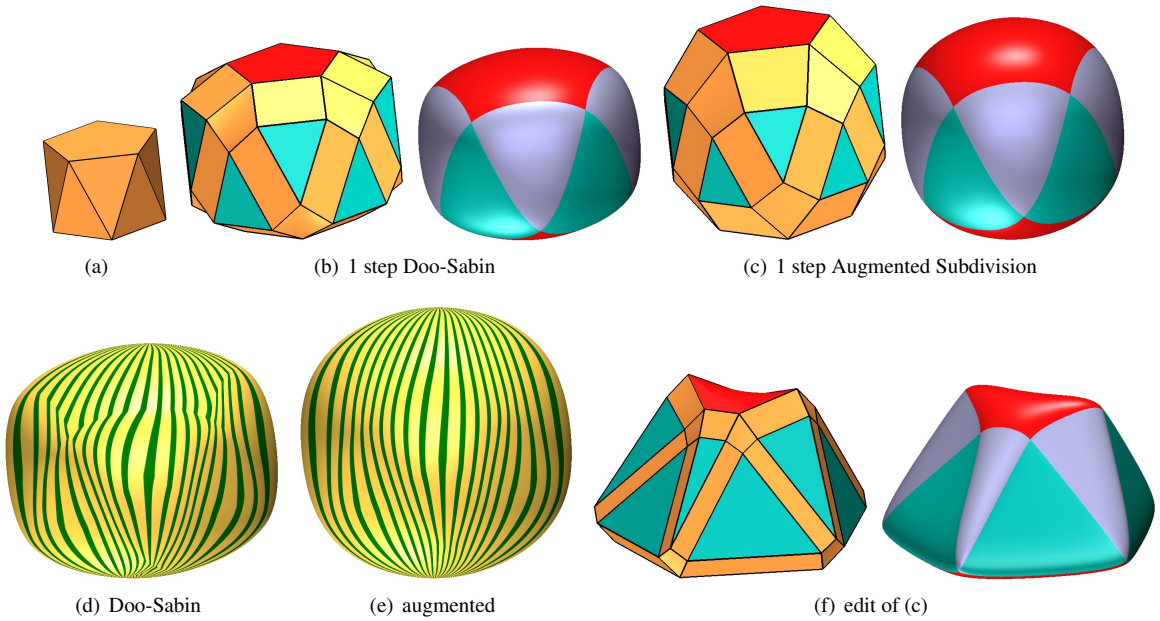

(a) (b) 1 step Doo-Sabin (c) 1 step Augmented Subdivision

(d) Doo-Sabin (e) augmented (f) edit of (c)

Figure 19: Comparison of G^1 joined caps $\mathbf{p}$ after one step of Doo-Sabin (b,d) vs Augmented Subdivision (c,e). (a) 5-sided antiprism: two 5-sided facets and 10 triangles.

the main body is C^1. Interrogation by highlight lines confirms that both primal and dual multi-sided surfaces are of high quality as in the earlier isolated examples. And while the primal construction yields good shape everywhere, quality problems in the dual construction can arise stemming from artifacts in the regular bi-2 splines that travel into the transition from the bi-2 to the multi-sided surface.

To illustrate how refined modeling can leverage the parametrically smooth transitions, Fig. 20 d illustrates localized embossing of the multi-sided surface Fig. 20 b. The groove in Fig. 20 h, along the transition rings and the regular bi-3 spline of surface Fig. 20 f, is a C^2 feature.

6.3. Concluding Remarks and Limitations

The presented construction unifies the treatment of multi-sided facets within a complex of 'primal', bicubic C^2-spline, repsectively 'dual', biquadratic C^1-spline surfaces. A key ingredient is a proto-map for a primal-dual agnostic guide. The n-sided rings naturally support refinement, that can be use for design, see Fig. 20 d,h, as well as for isogeometric analysis. [GP15] The structural similarity of the main body to the contracting rings of Catmull-Clark subdivision implies that the geometric modelling approach of [TAF16] can be applied. And while we can freely choose the main body to be C^2, the examples of Section 5 (see also [KP19]) show the quality of the simpler surfaces with C^1 bi-4 main body are superior to those with C^2 bi-4 main body.

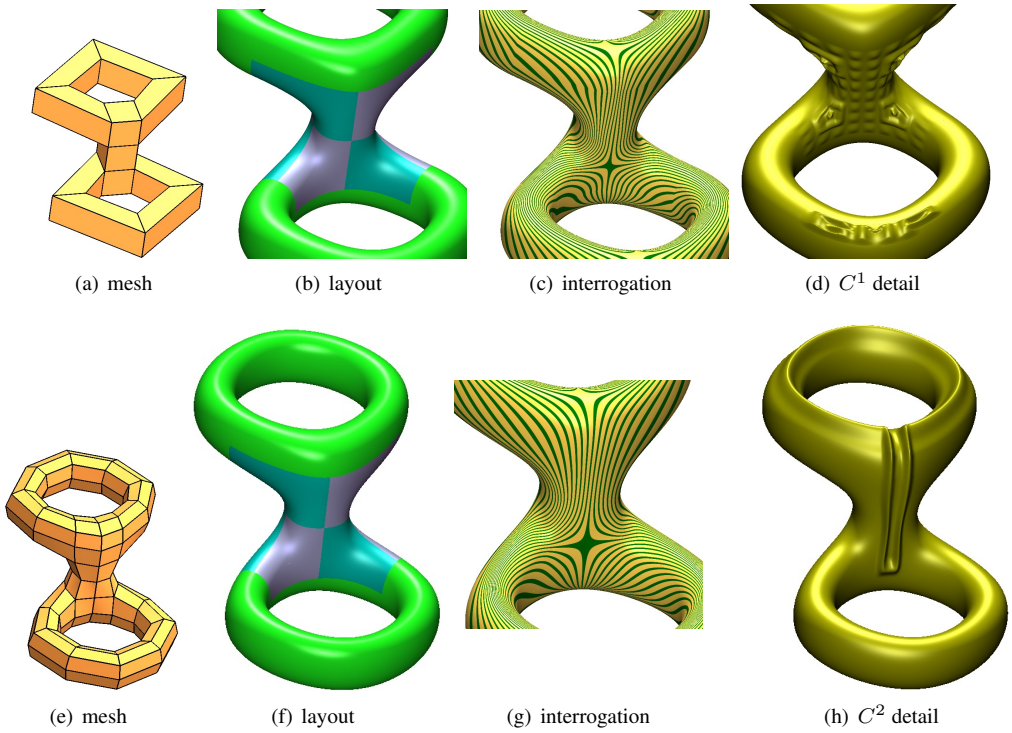

(a) mesh (b) layout (c) interrogation (d) C^1 detail

(e) mesh (f) layout (g) interrogation (h) C^2 detail

Figure 20: Genus 2: Smoothly blending two tori into an object of genus 2 via tightly placed (purple, blue) multi-sided caps. *top*: dual (bi-2) interpretation; *bottom*: primal (bi-3) interpretation of the input net. (d,h) Localized editing across the transition ring and the regular spline surface.

When the surrounding surface is bi-2, the surface degree can be reduced from bi-4 to bi-3. However numerous trials confirmed that satisfactory highlight line distributions then require a far more complex patch-layout of the multi-sided surfaces. [KP19] The unified construction can be extended to DS-nets in a C^2 bi-3 surface – but this requires a number of additional non-trivial tools beyond the scope of this paper.

Acknowledgements This work was supported in part by DARPA HR00111720031 and NIH R01 EB018625.

References

[ADS11] Ursula H. Augsdörfer, Neil A. Dodgson, and Malcolm A. Sabin. Artifact analysis on B-splines, box-splines and other surfaces defined by quadrilateral polyhedra. *Comp Aid Geom Design*, 28(3):177–197, 2011.

[BC94] Klaus-Peter Beier and Yifan Chen. Highlight-line algorithm for realtime surface-quality assessment. *Comp-Aid Design*, 26(4):268–277, 1994.

[CADS09] Thomas J. Cashman, Ursula H. Augsdörfer, Neil A. Dodgson, and Malcolm A. Sabin. NURBS with extraordinary points: high-degree, non-uniform, rational subdivision schemes. *ACM Tr Graph*, 28(3):46:1–46:9, 2009.

[CC78] E. Catmull and J. Clark. Recursively generated B-spline surfaces on arbitrary topological meshes. *Computer-Aided Design*, 10:350–355, September 1978.

[DS78] D. Doo and M. Sabin. Behaviour of recursive division surfaces near extraordinary points. *Computer-Aided Design*, 10:356–360, September 1978.

[Far88] Gerald Farin. *Curves and Surfaces for Computer Aided Geometric Design: A Practical Guide*. Academic Press, 1988.

[GP15] David Groisser and Jörg Peters. Matched G^k-constructions always yield C^k-continuous isogeometric elements. *Computer Aided Geometric Design*, 34:67–72, March 2015.

[HK18] Gerben J. Hettinga and Jirí Kosinka. Multisided generalisations of Gregory patches. *Computer Aided Geometric Design*, 62:166–180, 2018.

[HK20a] Gerben J. Hettinga and Jiri Kosinka. Multisided B-spline Patches Over Extraordinary Regions. In Silvia Biasotti, Ruggero Pintus, and Stefano Berretti, editors, *Smart Tools and Apps for Graphics - Eurographics Italian Chapter Conference*. The Eurographics Association, 2020.

[HK20b] Gerben J. Hettinga and Jirí Kosinka. A multisided C^2 B-spline patch over extraordinary vertices in quadrilateral meshes. *Comput. Aided Des*, 127:102855, 2020.

[HM90] Klaus Höllig and Harald Mögerle. G-splines. *Computer-Aided Geometric Design*, 7:197–207, 1990.

[KNP16] Kęstutis Karčiauskas, Thien Nguyen, and Jörg Peters. Generalizing bicubic splines for modelling and IGA with irregular layout. *Computer Aided Design*, 70:23–35, Jan 2016.

[KP07] Kęstutis Karčiauskas and Jörg Peters. Concentric tesselation maps and curvature continuous guided surfaces. *Computer Aided Geometric Design*, 24(2):99–111, Feb 2007.

[KP09] Kęstutis Karčiauskas and Jörg Peters. Adjustable speed surface subdivision. *Computer Aided Geometric Design.*, 26:962–969, 2009.

[KP15a] Kęstutis Karčiauskas and Jörg Peters. Improved shape for multi-surface blends. *Graphical Models*, 8:87–98, 2 2015.

[KP15b] Kęstutis Karčiauskas and Jörg Peters. Point-augmented biquadratic C^1 subdivision surfaces. *Graphical Models*, 77:18–26, Jan 2015.

[KP16] Kęstutis Karčiauskas and Jörg Peters. Minimal bi-6 G^2 completion of bicubic spline surfaces. *Computer Aided Geometric Design*, 41:10–22, Jan 2016.

[KP17] Kęstutis Karčiauskas and Jörg Peters. Refinable G^1 functions on G^1 free-form surfaces. *Computer Aided Geometric Design*, 54:61–73, May 2017.

[KP18] Kęstutis Karčiauskas and Jörg Peters. Fair free-form surfaces that are almost everywhere parametrically C^2. *Journal of Computational and Applied Mathematics*, pages 1–10, 2018.

[KP19] Kęstutis Karčiauskas and Jörg Peters. Curvature-bounded guided subdivision: biquartics vs bicubics. *Computer Aided Design*, pages 1–11, Jul 2019.

[KP20] Kęstutis Karčiauskas and Jörg Peters. Least degree G^1-refinable multi-sided surfaces suitable for inclusion into C^1 bi-2 splines. *CAD*, to appear:1–12, 2020. PMC7505230.

[KPR04] K. Karciauskas, J. Peters, and U. Reif. Shape characterization of subdivision surfaces – case studies. *Computer-Aided Geometric Design*, 21(6):601–614, july 2004.

[LFS16] X. Li, G. Finnigan, and Thomas Sederberg. G^1 non-uniform catmull-clark surfaces. *ACM Transactions on Graphics*, 35:1–8, 07 2016.

[LS08] Charles T. Loop and Scott Schaefer. G^2 tensor product splines over extraordinary vertices. *Comput. Graph. Forum*, 27(5):1373–1382, 2008.

[MM18] Yue Ma and WeiYin Ma. Subdivision schemes with optimal bounded curvature near extraordinary vertices. *Computer Graphics Forum*, 37(7):455–467, Oct 2018.

[NKP16] Thien Nguyen, Kęstutis Karčiauskas, and Jörg Peters. C^1 finite elements on non-tensor-product 2d and 3d manifolds. *Applied Mathematics and Computation*, 272(1):148–158, 2016.

[Pet02] J. Peters. Geometric continuity. In *Handbook of Computer Aided Geometric Design*, pages 193–229. Elsevier, 2002.

[SV18] Péter Salvi and Tamás Várady. Multi-sided bézier surfaces over concave polygonal domains. *Comput. Graph*, 74:56–65, 2018.

[SVR14] Péter Salvi, Tamás Várady, and Alyn P. Rockwood. Ribbon-based transfinite surfaces. *Comput. Aided Geom. Des*, 31(9):613–630, 2014.

[TAF16] Wolfgang Thaller, Ursula Augsdörfer, and Dieter W. Fellner. Procedural mesh features applied to subdivision surfaces using graph grammars. *Computers & Graphics*, 58:184 – 192, 2016. Shape Modeling International 2016.

[TSH+20] Deepesh Toshniwal, Hendrik Speleers, René R. Hiemstra, Carla Manni, and Thomas J.R. Hughes. Multi-degree B-splines: Algorithmic computation and properties. *Computer Aided Geometric Design*, 76:101792, 2020.

[VSR12] Tamás Várady, Péter Salvi, and Alyn P. Rockwood. Transfinite surface interpolation with interior control. *Graph. Model*, 74(6):311–320, 2012.